Article:
Jin, H, Lin, G, Zeiny, A et al. (2 more authors) (2019) Nanoparticle-based solar vapor generation: An experimental and numerical study. Energy, 178. pp. 447-459. ISSN 0360-5442

https://doi.org/10.1016/j.energy.2019.04.085

Nanoparticle-based solar vapor generation: an experimental and numerical study

Haichuan Jin[a], Guiping Lin[a], Aimen Zeiny[b,c], Lizhan Bai[a], Dongsheng Wen[a,b,*]

[a]*Laboratory of Fundamental Science on Ergonomics and Environmental Control, School of Aeronautic Science and Engineering, Beihang University, Beijing 100191, PR China*

[b]*School of Chemical and Process Engineering, University of Leeds, Leeds, LS2 9JT UK*

[c]*Department of Mechanical Engineering, Faculty of engineering, University of Kufa, Iraq*

Abstract: Steam generation of nanofluid under solar radiation has attracted intensive attention from researchers. Due to strong absorption of solar energy, nanoparticle-based solar vapor generation is promising in desalination, sterilization and producing steam for electricity generation. Steam generation for different concentrations of gold nanoparticle dispersions under focused sunlight of 5 sun and 10 sun were performed in this paper. A numerical model combining radiative heat transfer, moisture transport, and laminar flow was built to investigate the temperature profile, evaporation rate above the surface and radiative intensity distribution inside the nanofluid. We found that localized energy trapping at the surface of nanofluid was responsible for the fast vapor generation. To convert more solar radiative energy into latent heat of water (i.e., to vaporize water) at the surface, a new method was proposed to optimize the range of nanofluid concentration and optical depth for solar vapor generation design.

Keywords: nanoparticle, solar vapor generation, radiative intensity, solar energy

* Corresponding author: E-mail address: d.wen@leeds.ac.uk

1. Introduction

Since the propose of solar steam generation enabled by nanoparticle recent years [1–10], it has attracted substantial interest due to its efficient solar energy harvesting and remarkable steam production rate. Combining steam generation with abundant solar energy is essential for a wide range of applications, such as solar-refrigeration systems, desalination unit, large scale electricity generation, and corresponding compact small scale systems such as sterilization and clearing [11–15]. Volumetric solar energy absorption which contains certain materials seeded in a working fluid to convert solar radiative energy to thermal form within the fluid itself originated in the 1970s, with the purpose of absorbing more solar energy and minimizing the surface temperature of receivers, forming a 'thermal trapping' phenomenon [16]. It has been reported that nanoparticle-based fluid (i.e., nanofluid) can improve radiative absorbing efficiency significantly [4,17–24] because of the unique optical properties of particles at the nanoscale. Intensive investigations have been carried out using metal (such as Cu, Au, and Ag), metal oxide (such as TiO_2, Al_2O_3) and carbon materials [25–29], both under laboratory [4,30–32] and natural sunlight conditions [1,6,33]. Very recently, nanoparticles have been introduced as roles which not only heat the based fluids but also directly generate steam consuming solar energy [1–4,29,34–36]. Direct steam production efficiency as much as 80% has been reported [1,6] at 1000 times concentrated solar intensity, under subcooling condition (i.e., the bulk temperature is still ~6 ℃), even only 20% of the solar radiation was used to increase the bulk fluid temperature. One hypothesized explanation is that rapidly heating of nanoparticles produced nanobubbles directly around nanoparticles, and the rise of bubbles to the surface of the liquid leads to the release of the vapor produced [37–39], numerical work [1,35,40] supports the possibility of nanobubble formation based on non-equilibrium phase change assumption. Under very intense laser heating condition (i.e., 100~10000

MW/m^2), both experimental and theoretical work has confirmed the nanobubble formation [19,40–43]. However, the issue whether nanoparticle dispersion under typical concentrated solar flux (i.e., typically <1 MW/m^2) can introduce nanobubbles and the resulting high consumed radiative energy percentage of evaporation even steam generation is still under intense debate. Another up to date mechanism [2–4] employs classical Fourier-law heat conduction to describe the direct steam generation phenomenon based on nanofluid adequately. According to our previous research [44], steam generation is mainly caused by localized boiling and evaporation in superheated regimes due to a highly non-uniform temperature distribution, albeit the bulk fluid is still subcooled. Such a phenomenon can be explained by the classical heat transfer theory and the hypothesized 'nanobubble', i.e., steam produced around heated particles was unlikely to occur under normal solar concentrations.

For those experiments [45] where the radiative intensity is under 50 sun (i.e., less than 5×10^4 W/m^2), the highest temperature of nanofluid is challenging to reach the boiling point. Vaporized water generates through surface evaporation instead of localized boiling. Solar vapor generation of nanofluid under solar radiation is a complex physical process which combines radiative transfer in participating media, heat transfer with phase change (i.e., evaporation at the surface), moisture transport in air and laminar flow with buoyancy force. Such a complicated process is difficult to simulate, especially when these multi-physical processes couple with each other. Most of the previous investigations concentrate on the vaporized mass change, and evaporation efficiency and the majority of these works are experiments. The radiative intensity distribution inside the nanofluid is rarely investigated [4,46–48]. The radiation intensity is especially sensitive to the concentration of nanofluid and the optical depth. The radiative heat transfer process can be comprehensively studied through simulations, which has yet to be established.

In this paper, enhance solar vapor generation by seeding nanoparticles into a volumetric absorption receiver were investigated both experimentally and numerically. Gold nanofluid with different concentrations was prepared, and the solar vapor generation experiments were performed under different solar intensity (i.e., 5 sun and 10 sun). Vaporized mass change and temperature distribution with multiple thermocouples were recorded. The evaporation (latent heat) efficiency and temperature increase (sensible heat) efficiency with the concentration of nanofluid were carefully investigated. Together with numerical results, the radiative energy distribution inside nanofluid was discussed. A new numerical method was proposed to optimize nanofluid concentration and optical depth to obtain the effective evaporation rate for nanofluid under solar radiation. The novelty of this work is that the reason for fast vapor generation of nanofluid under solar radiation has been revealed through experiments and simulations. For the first time, a 3D simulative model has been established, which comprehensively describes the radiative heat transfer, evaporation and vapor-flow process for nanofluid under solar radiation.

2. Experimental details and methods

2.1. Experimental Setup and Data Acquiring

The experiments were performed under concentrated solar irradiation from a solar simulator (Oriel Sol3A with an output beam size of $101.6\,\text{mm} \times 101.6\,\text{mm}$) (**Fig. 1B)**. Diluted gold nanoparticle suspensions together with DI water were placed into the testing container (i.e., with a diameter of 30 mm) separately. A Fresnel lens (Shenzhen MEIYING Technology CO., LTD) with a 200 mm focal distance was used to focus the sunlight. A digital weighing scale (Ohaus Discovery Model DV214c) with precision of $\pm\,0.0005$ g was used to measure evaporated mass change. To investigate non-uniform temperature distribution inside the samples, 8 type K thermocouples (Omega CHAL-002) with a precision of $\pm 0.5°C$ were used, as shown in **Fig. 1A**.

Among those six thermocouples were put inside the solar receiver to measure the temperature gradient, named TC1-TC6 from bottom to the surface. One thermocouple located above the surface of the testing sample, name as TC7. Another was used to measure the ambient temperature, named as TC0. A data acquisition system (National Instruments^{TM} SCXI-1000 with SCXI-1102 Voltage input module) was used to record the readings from thermocouples and digital weighing scale. Before the experiment, all the receiver was washed carefully with pure water of ambient temperature, all samples were put inside a fridge and maintained the same starting temperature (20 ℃). During the preparation, all gold nanofluids were avoided to expose to sunlight.

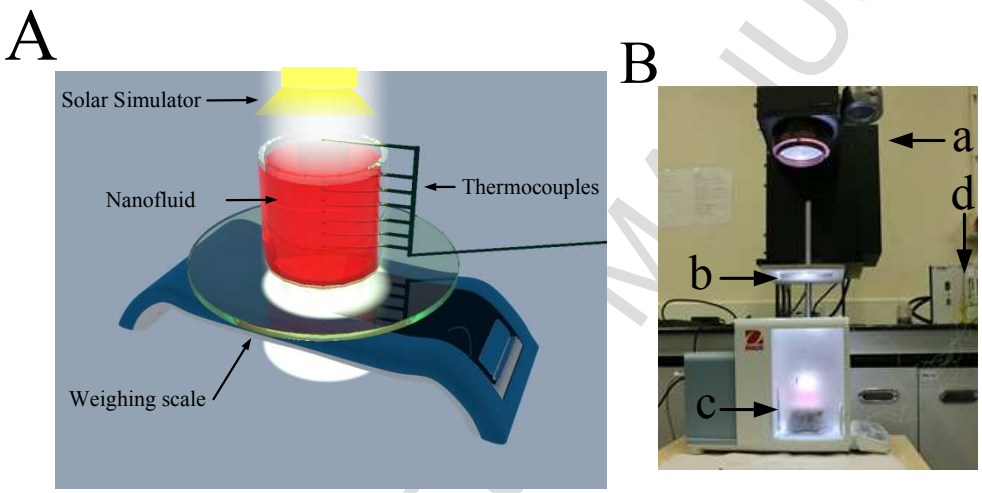

C

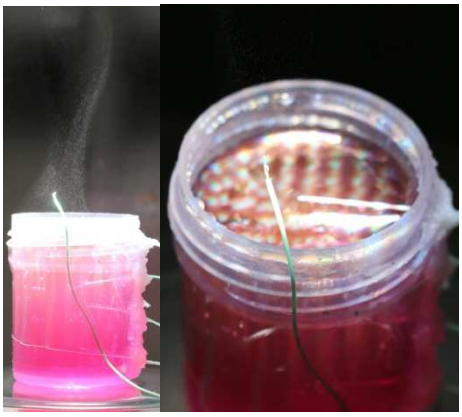

Fig. 1. (**A**) Schematics of experimental setting for solar-driven evaporation. 6 thermocouples (TC1~TC6 from bottom to the surface) are used to measure temperature gradient inside illuminated nanofluid. One thermocouple (TC7) was above the surface, another thermocouple (TC0) was to measure the ambient temperature. (**B**) Photo for experiment setup. **a** was the solar simulator, **b** was the Fresnel Lens, **c** was the digital weighing scale with four digits, **d** was the data acquisition system. (**C**) Photo of Au nanofluid (5 ppm) under 10 sun solar radiation.

2.2. Preparation of Au nanofluids

A one-step method [49] was employed to produce stable gold nanoparticle suspensions. Here 5×10^{-6} mol $HAuCl_4$ was dispersed into 190 ml DI water in a three-necked flask. A magnetic blender with a heating source was used to stir the liquid until boiling. Boiling was continued for 10 mins and 10 ml of 0.5% sodium citrate was subsequently added. The solution turned dark blue within 30 s, and the final color became wine red after being heated for an additional 20 mins. The dispersions were maintained good stability for over two months and used for the below experiments without further purification and separation. Particle size and shape was characterized (**Fig. 2A**) by a Transmission Electron Microscopy (TEM) (FEI Tecnai TF20: FEGTEM Field

emission gun TEM/STEM fitted with HAADF detector, Oxford Instruments INCA 350 EDX system/80mm X-Max SDD detector and Gatan Orius SC600A CCD camera).

The optical property of gold nanofluids was characterized by a UV-spectrophotometer (Shimadzu UV-1800). A dynamic light scattering (DLS) device (Malvern nanosizer) was employed to identify the particle size distribution, which can be seen from **Fig. 2B**.

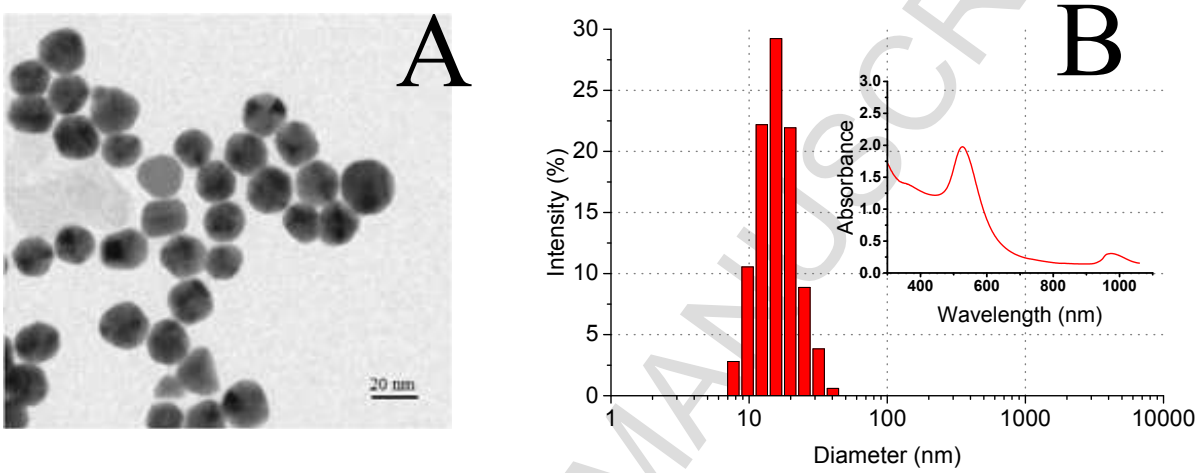

Fig. 2. (**A**) TEM image of the gold nanoparticle; (**B**) Particle size distribution and UV-Vis result (inset) of gold nanofluid with a concentration of 5 ppm

3. Experimental results and analysis

3.1. Temperature profile and evaporated mass change

Once the tube was illuminated under 5 sun, the bulk temperature of nanofluids and DI water increased (**Fig. 3**). For DI water (**Fig. 3A**), the temperature increased slowly and reached only 41 ℃ after 40 minutes illumination. Only 0.6 g water was evaporated during 40 minutes, and the maximum evaporation rate reached only 0.23 mg/s. In the first 20 minutes, the temperature inside the volume was non-uniform, and the largest temperature difference was 5 ℃. That is because solar intensity decreases along the optical depth, resulting in higher absorption at the surface. After then, temperature gradient shrinks to less than 2 ℃, indicating higher surface evaporation rate

reduced the surface temperature increasing rate, leading a more uniform temperature profile. All nanofluids reached a higher surface temperature than that of water. Temperature gradient increased with volume concentration, which meant temperature inside nanofluids became more non-uniform when more particles exist inside the receiver. The highest temperature (TC6) was elevated compared with water, but for different concentration of nanofluids, the highest temperature was almost the same (i.e., 60 ℃). However, the lowest temperature decreased when the concentration increased (except for water), for example, TC6=44 ℃ at $t = 40$ min for 1 ppm gold nanofluid, but TC6=30 ℃ at $t = 40$ min for 12.5 ppm gold nanofluid. Evaporated mass change and evaporation rate were significantly increased when adding gold nanoparticles inside water receiver. The highest evaporation rate reached 0.65 mg/s for 12.5 ppm gold nanofluid, almost 3 times of that of DI water. Evaporation rate slightly increased with nanofluids concentration.

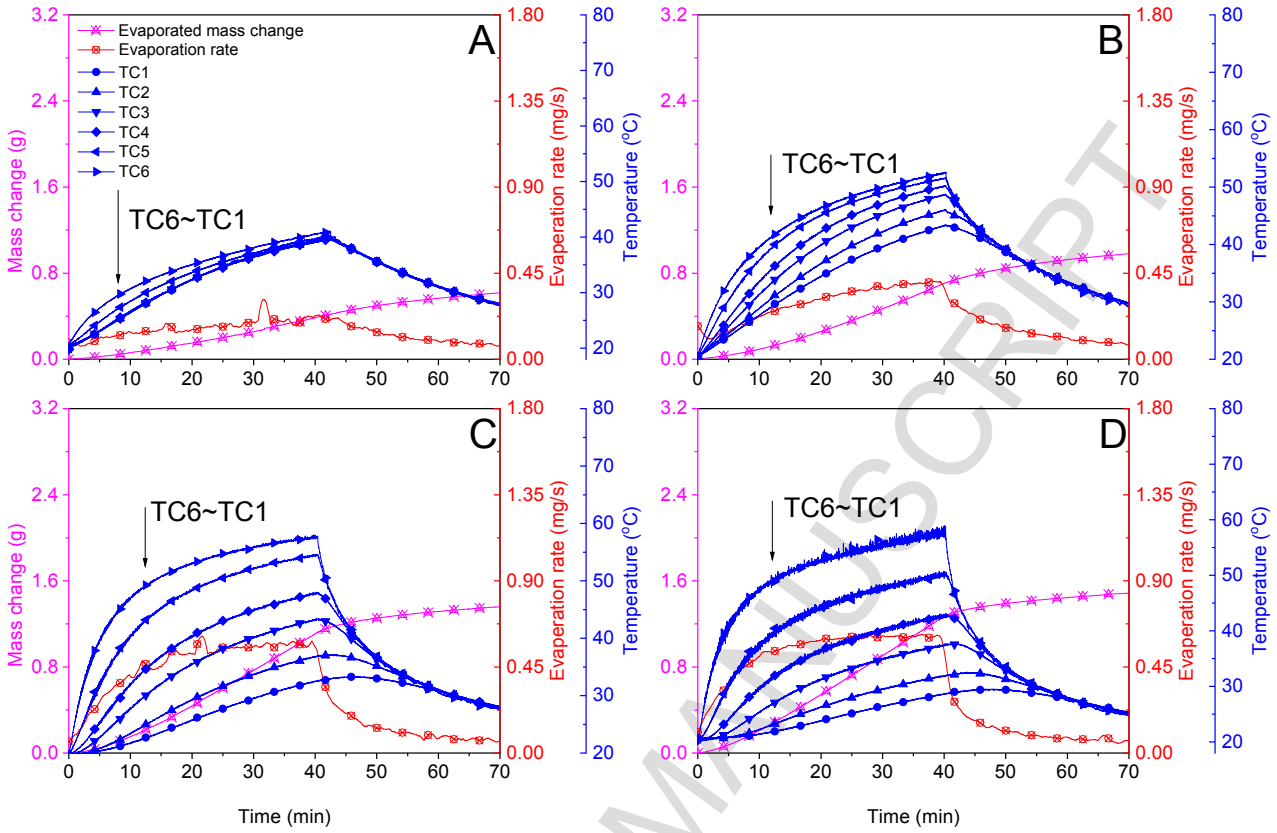

Fig. 3. Comparison of experimental obtained increasing temperature, mass change, the evaporation rate with different volume concentrations of gold nanofluids and DI water under 5 sun. (**A**) DI water; (**B**)1 ppm; (**C**)5 ppm; (**D**) 12.5 ppm. After 40 minutes, the solar simulator was shut down, and samples stayed for cooling down.

More energy was consumed to evaporate water inside nanofluids. According to radiative heat transfer process [50], more solar radiative energy was converted to thermal form when the concentration of fluid increased. However, according to **Fig. 3B, C, D**, the highest temperature of different concentration nanofluids was almost the same, but the lower bulk temperature was found when the concentration was increased, indicating that the obtained sensible heat was less when the concentration was higher. Although heat loss would be more significant for higher temperature,

one conclusion based on this phenomenon was: increasing concentration increased the percentage of energy consumption in evaporating water. Further investigation can be seen in **section 5**. After the solar simulator was shut down, all thermocouples reached the same temperature after a short time (i.e., 5 minutes for 5 ppm).

In order to investigate the role of solar radiation in heating nanofluids and evaporating water into the air, experiments under 10 sun were performed under the same operating conditions (**Fig. 4**). High solar radiative intensity increased the whole temperature level of both water and nanofluid. For example, the temperature of TC1 and TC6 for the concentration of 1 ppm under 10 sun were 60 ℃ and 70 ℃, respectively; they were 44 ℃ and 53 ℃ for the same concentration but under 5 sun. The increasing of solar radiative intensity accelerated the evaporation rate significantly for both of DI water and nanofluids. For a concentration of 12.5 ppm nanofluid, evaporation rate at $t = 40$ min was 1.45 mg/s under 10 sun, more than twice of that under 5 sun. The non-uniformity was amplified when the solar radiative intensity was increased. For example, the maximum temperature difference was 30 ℃ for the concentration of 5 ppm under 5 sun, but it was 35 ℃ when under 10 sun. Actuarially, the temperature at the surface was not the highest along the optical depth. Due to strong evaporation at the surface, large amount of absorbed solar energy at the surface will be converted into latent heat, which will cause that the heat transfer direction is towards the surface inside nanofluid. This will be explained in **section 5**. Once evaporated water reached a certain amount, the interface level of samples and air descended and finally TC6 represented the exact temperature of the interface. After about 20 minutes, the fluctuation of temperature happens for TC6 in **Fig. 4C** and **D**. This is due to that the thermocouple of the up layer (TC6) was exposed to air. (i.e., 30 min for 5 ppm gold nanofluid, **Fig. 4C**). Due to surface

evaporation and vapor flow, water will condensate at the surface of TC6, which causes the fluctuation of temperature of TC6.

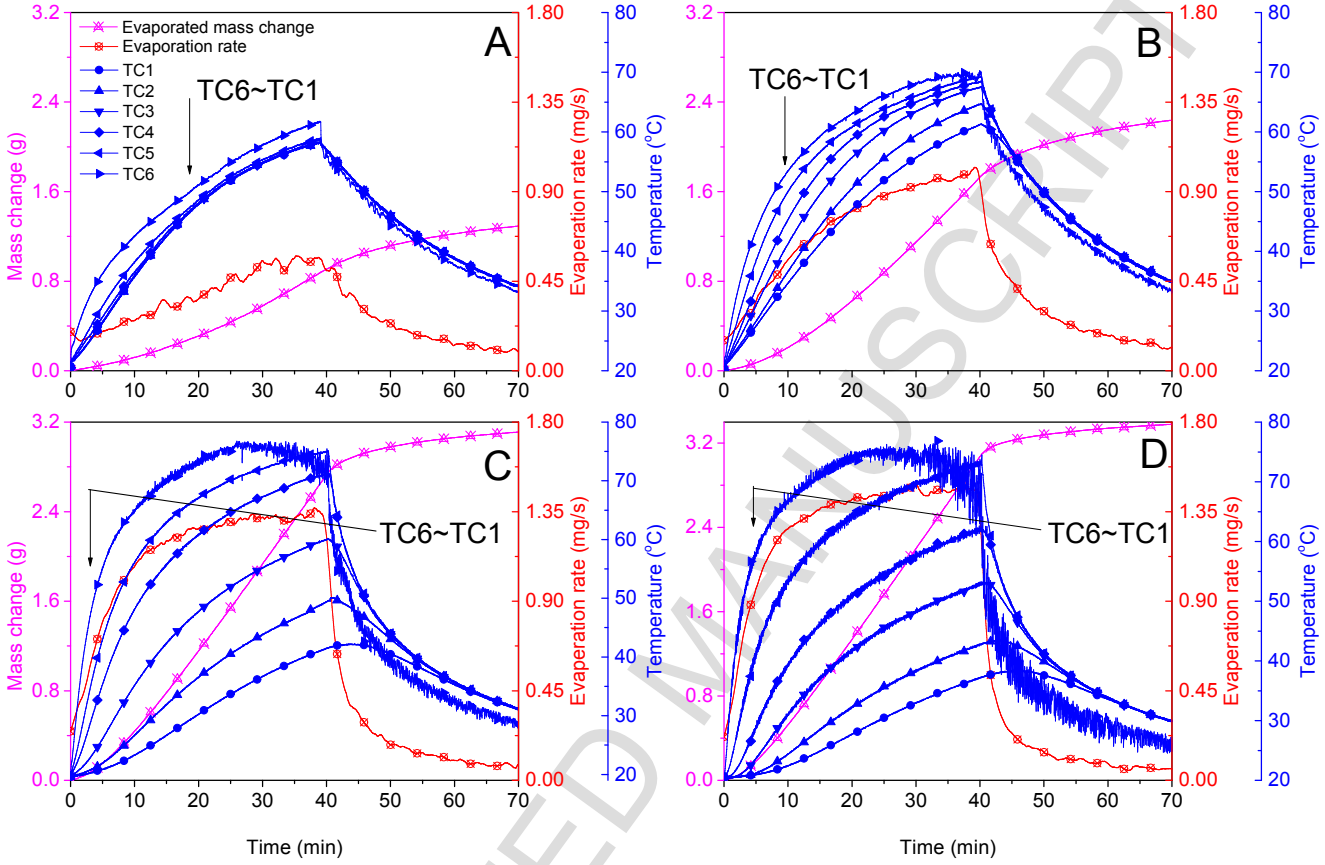

Fig. 4. Comparison of experimental obtained temperature, mass change, evaporation rate with different volume concentrations of gold nanofluids and DI water under 10 sun illumination. (**A**) DI water; (**B**) 1 ppm; (**C**) 5 ppm; (**D**) 12 ppm. After 40 minutes, the solar simulator was shut down, and samples stayed for cooling down.

3.2. Heating and evaporation efficiency

In order to investigate the energy consumption, surface and bottom temperature were presented (**Fig. 5**). Only for 1 ppm nanofluid, the bottom temperature was higher than that of water during heating up under both 5 sun (**Fig. 5A**). Increasing concentration of nanofluid decreased the bottom

temperature under 10 sun (**Fig. 5C**). This can be explained: higher concentration would lead to a localized sunlight absorption of the surface layer, resulting in a poor energy absorption under the bottom. The non-uniform distribution of radiative intensity will cause non-uniform temperature distribution. The radiative intensity distribution along the optical depth will be carefully discussed in **section 5**.

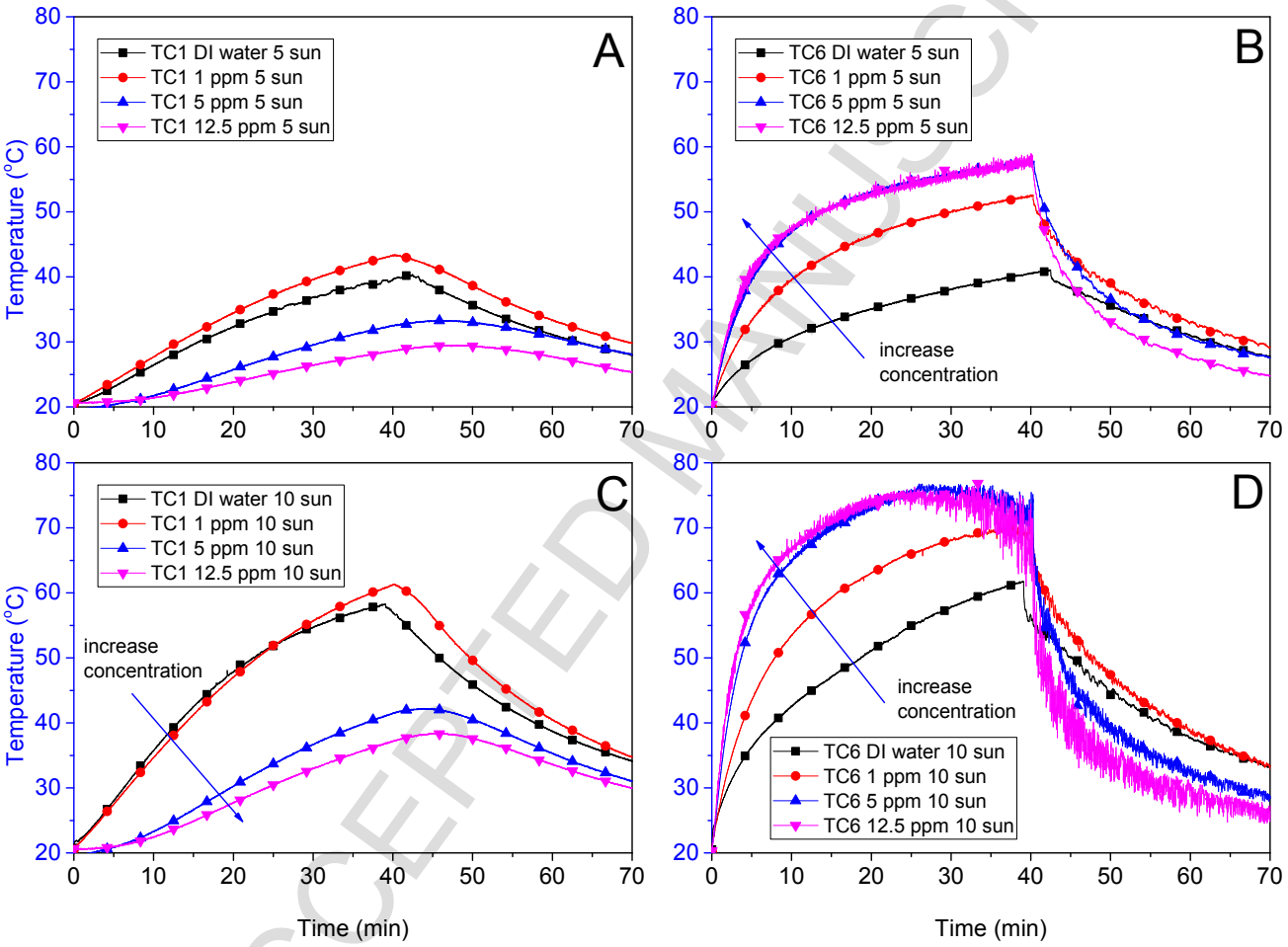

Fig. 5. Bottom temperature (TC1) (**A**, **C**) and surface temperature (TC6) (**B**, **D**) of different concentrations with time under both 5 sun (**A**, **B**) and 10 sun (**C**, **D**)

Increasing solar intensity would amplify temperature difference between different concentrations. More solar energy was absorbed, but the energy distribution was more non-

uniform. Adding nanoparticles into fluid increased the surface temperature significantly (**Fig. 5BD**). But for 5 ppm and 12.5 ppm nanofluids, they had almost the same surface temperature. The detailed explaination can be seen in the numerical results in **section 5**.

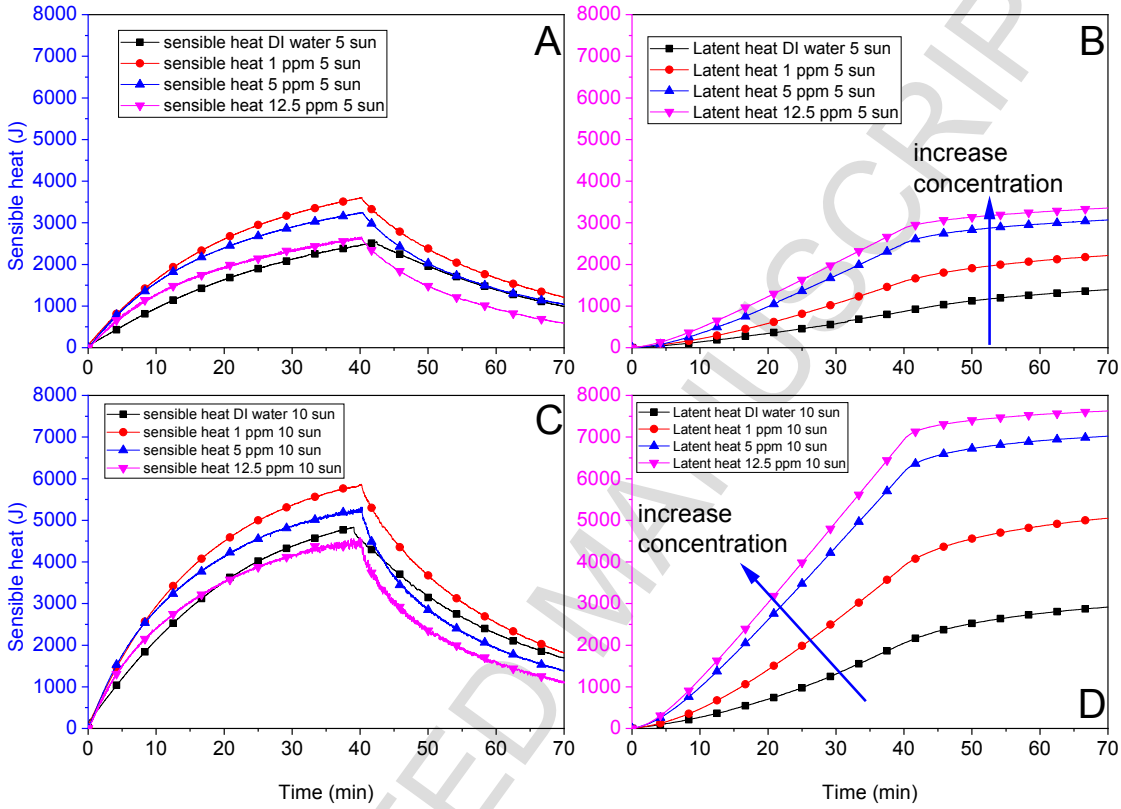

Fig. 6. Sensible heat (**A**, **C**) and latent heat (**B**, **D**) of different concentrations with time under both 5 sun (**A**, **B**) and 10 sun (**C**, **D**).

Sensible heat and latent heat have been calculated according to the equations below:

$$Q_{\text{sensible}} = (c_w m_w + c_n m_n)\Delta\overline{T} \approx c_w m_w \Delta\overline{T} = c_w m_w \sum_{\text{n}=1}^{\text{n}=6} \Delta T_{\text{n}}/6 \tag{1}$$

$$\frac{U_{Q_{\text{sensible}}}}{Q_{\text{sensible}}} = \sqrt{\left(\frac{U_m}{m_w}\right)^2 + 6\left(\frac{U_T}{\sum_{\text{n}=1}^{\text{n}=6}\Delta T_{\text{n}}}\right)^2} \tag{2}$$

$$Q_{\text{latent}} = \text{L}\Delta m_w \tag{3}$$

$$U_{Q_{\text{latent}}} = \text{L}U_m \tag{4}$$

where L is the latent heat of evaporation of water. m_w and m_n are the mass of water and nanoparticles in nanofluid, respectively. Comparing with the base fluid, thermal energy stored in the gold nanoparticles is negligible owing to its extremely low concentration, i.e., a maximum of 25 ppm in volume (0.048% in mass). Based on the standard error analysis method [51], the uncertainty for sensible heat and latent heat can be calculated in Equation 2 and 4. The maximum uncertainty of sensible heat and latent heat are: $U_{Q_{\text{sensible}}}|_{\max} = 27.51$ J, $U_{Q_{\text{latent}}}|_{\max} = 1.13$ J.

Adding nanoparticles into fluid increased both of the obtained sensible heat and latent heat, and the higher concentration of nanofluid got more latent heat. However, in relation to the converted sensible heat, it decreases with higher concentrations in the nanofluid. Surprisingly, for 12.5 ppm nanofluid under 10 sun (**Fig. 6C**), the sensible heat was lower than that of water under the same solar intensity. Increasing solar intensity would increase the latent heat significantly but slightly increased the sensible heat. Increasing solar intensity would also amplify the difference of latent heat among different concentrations.

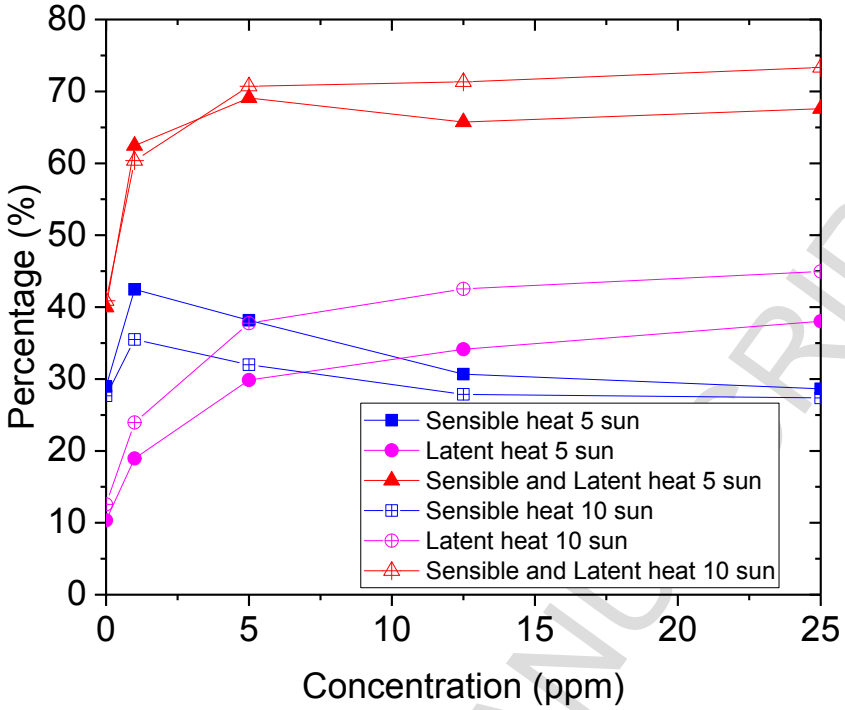

Fig. 7. Energy consumption percentage of sensible heat and latent heat with volume concentration under 5 sun and 10 sun.

In order to investigate the energy conversion efficiency, percentage sensible heat and latent heat with concentration under both 5 sun and 10 sun were investigated (**Fig. 7**). Adding nanoparticles into fluid significantly increases total energy absorption from solar radiative energy (see sensible heat and latent heat). Increasing concentration slightly increases energy conversion efficiency, which was consistent with our previous research [32,33]. Increasing concentration would increase latent heat but decrease sensible heat efficiency. The nanofluid with high concentration absorbed more solar energy and consumed it to evaporate water. With higher solar intensity, the latent heat and total efficiency were increased but the sensible heat efficiency was decreased. Based on the experimental results, gold nanoparticles inside water could increase photothermal conversion

efficiency and evaporate more water with lower bulk temperature under the current experimental settings in this paper.

4. A numerical model of nanoparticle-based solar vapor generation

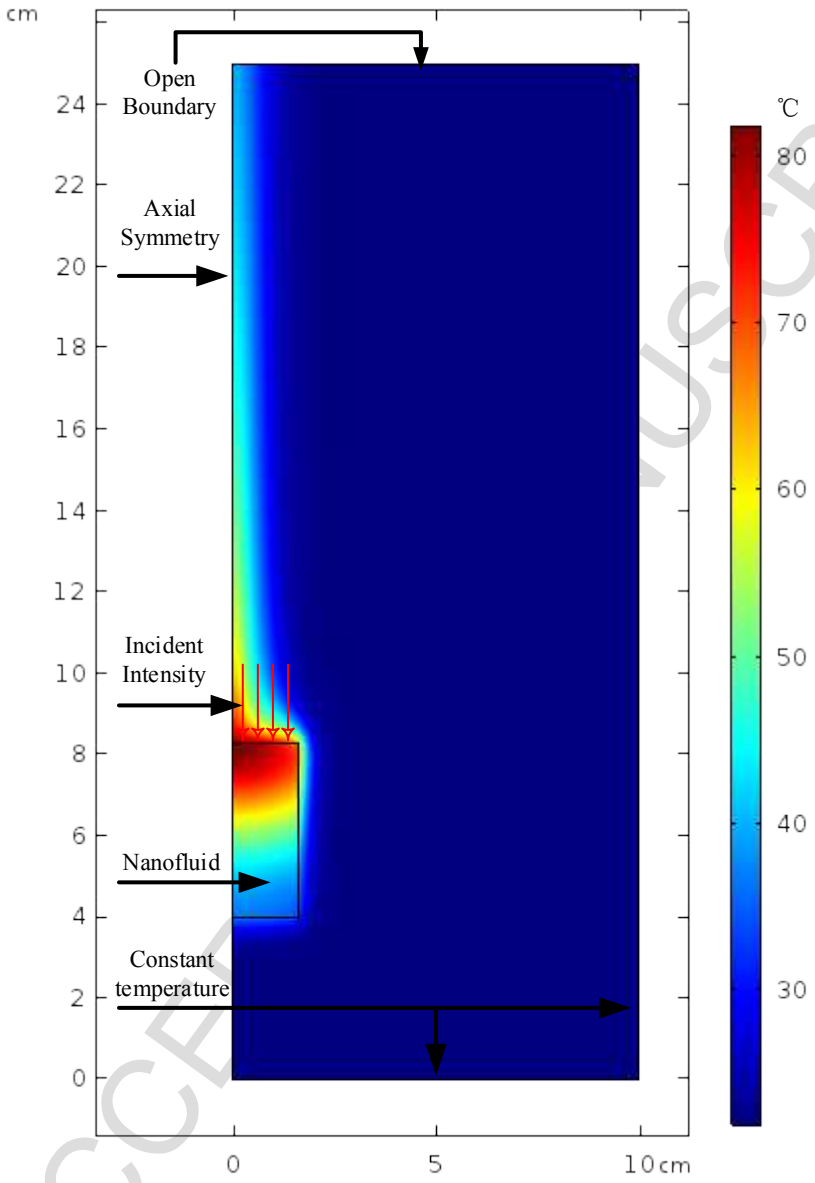

Fig. 8. A numerical model of nanoparticle-based solar vapor generation

The experiment in this paper relates to several physical processes: 1) Nanofluid absorbs solar energy and converts it into thermal form; 2) phase change of water at the interface between

nanofluid and air; 3) evaporated moisture flows upwards due to buoyancy force and accelerate the evaporation. A 3-D numerical model to simulate the evaporation process was built through COMSOL Multiphysics®, as shown in **Fig. 8**. Radiation in Absorption-Scattering Media (RASM) model, Heat Transfer in fluid (HT) model, Moisture Transport in air (MT) model, and Laminar Flow (SPF) model were employed. The Multiphysics of Heat Transfer with Radiation in Absorbing-Scattering Media (HTRASM) was added to combine heat transfer equations and radiative transfer equations. Nonisothermal Flow (NITF) was selected to couple laminar flow and heat transfer of air inside the balance. Heat and Moisture (HAM) was added to couple heat and mass transfer, which includes evaporation induced latent heat source on the surface of nanofluid. Moisture Flow (MF) was added to couple laminar flow and moisture transport. The COMSOL Multiphysics®, a commercial software with finite element method (FEM) was employed to build up numerical model.

4.1. Solar radiation and radiative heat transfer

Similar with our previous work [52], actual solar irradiation profile was employed based on the ASTM G173-03 Reference Spectra [53]. Mie scattering approximation was selected to calculate the absorption and scattering coefficient [50]:

$$a_n = \frac{m\psi_n(mx)\psi_n'(x) - \psi_n(x)\psi_n'(mx)}{m\psi_n(mx)\xi_n'(x) - \xi_n(x)\psi_n'(mx)} \tag{5}$$

$$b_n = \frac{\psi_n(mx)\psi_n'(x) - m\psi_n(x)\psi_n'(mx)}{\psi_n(mx)\xi_n'(x) - m\xi_n(x)\psi_n'(mx)} \tag{6}$$

$$Q_{sca}(\lambda) = \frac{2}{x^2}\sum_{n=1}^{\infty}(2n+1)\left[|a_n|^2 + |b_n|^2\right] \tag{7}$$

$$Q_{ext}(\lambda) = \frac{2}{x^2}\sum_{n=1}^{\infty}(2n+1)\mathrm{Re}(a_n + b_n) \tag{8}$$

$$Q_{ext}(\lambda) = Q_{abs}(\lambda) + Q_{sca}(\lambda) \tag{9}$$

where the functions $\psi_n(x)$ and $\xi_n(x)$ are spherical Bessel functions [50]. The characteristic size in the radiative transfer equation is calculated as $x_\lambda = \pi D / \lambda$, where D represents the diameter of the nanoparticles. *m* represents the ratio of refractive indexes, calculated by:

$$m = \frac{n_{particles}}{n_{fluid}} \tag{10}$$

where $n_{particles}$ and n_{fluid} are the complex refractive index [54–56] of gold and based fluid relative to the ambient medium, respectively. The absorption coefficient is calculated from the equation below:

$$\kappa(\lambda) = \kappa_p(\lambda) + \kappa_f(\lambda) = \frac{3\pi}{2}\frac{f_v Q_{abs}(\lambda)}{D} + \frac{4\pi k_f(\lambda)}{\lambda} \tag{11}$$

$$\sigma(\lambda) = \frac{3\pi}{2}\frac{f_v Q_{sca}(\lambda)}{D} \tag{12}$$

The spectral intensity is described by the radiative transfer equation, known as RTE[50]:

$$\hat{s}\cdot\nabla I_\eta = \kappa_\eta I_{b\eta} - \beta_\eta I_\eta + \frac{\sigma_\eta}{4\pi}\int_{4\pi} I_\eta(\hat{s}_i)\Phi_\eta(\hat{s}_i,\hat{s})\,d\Omega_i \tag{13}$$

$$\nabla\cdot q_\eta = \kappa_\eta\left(4\pi I_{b\eta} - \int_{4\pi} I_\eta d\Omega\right) \tag{14}$$

$$\beta_\eta = \kappa_\eta + \sigma_\eta \tag{15}$$

where I_η is the radiative intensity of wavelength range $\lambda_{\eta_1} \to \lambda_{\eta_2}$ in the direction $\hat{s}_i$, $I_{b\eta}$ is the re-emission of nanofluid, $\Phi_\eta(\hat{s}_i,\hat{s})$ was called the scattering phase function, which described the probability of a ray from one direction $\hat{s}_i$ scattered into another direction $\hat{s}$; and κ_η, β_η and σ_η

are the absorption, extinction and scattering coefficient, respectively. The spectral radiative heat flux q_η is obtained by integrating the radiative intensity with the solid angle Ω.

As the absorption coefficient is wavelength dependent, the RTE equation is also wavelength dependent, which causes the computational difficulties when combining the RTE and heat transfer equations. What's more, most of the commercial FEM (Finite Element Method) or FVM (Finite Volume Method) software employs constant absorption coefficient (where σ is not wavelength dependent). In order to simplify the RTE and heat transfer equations, the wavelength dependent absorption coefficient is converted to optical depth dependent.

According to our previous research [52], a simplified model which can predict solar absorption efficiency has been proposed:

$$\eta\left(L,f_v\right)=\frac{\int_{0.2\mu m}^{3\mu m}E_0\left(\lambda\right)\left(1-10^{-A(\lambda)\frac{L}{L_0}}\right)d\lambda}{\int_{0.2\mu m}^{3\mu m}E_0\left(\lambda\right)d\lambda}=\frac{\int_{0.2\mu m}^{3\mu m}E_0\left(\lambda\right)\left(1-e^{-\kappa(\lambda,\ f_v)L}\right)d\lambda}{\int_{0.2\mu m}^{3\mu m}E_0\left(\lambda\right)d\lambda} \tag{16}$$

where $\eta\left(L,f_v\right)$ is the predicted photothermal conversion efficiency, which is a function optical depth L and volume concentration of nanofluid. $E_0\left(\lambda\right)$ represents the incident spectral emissive power, $A\left(\lambda\right)$ is the absorbance from UV-Vis spectrophotometer. The optical depth L is divided into a certain number of equal parts (with space step $\Delta z = 0.01$ mm) and the spectral emissive power (the unit is $W/m^2 \cdot m$) passing each part is named as $E_0\left(\lambda\right), E_1\left(\lambda\right)\cdots E_n\left(\lambda\right), E_{n+1}\left(\lambda\right)\cdots E_N\left(\lambda\right)$ (the unit is $W/m^2 \cdot m$), the radiative intensity (the unit is W/m^2) passing each part is named as $I_0, I_1 \cdots I_n, I_{n+1} \cdots I_N$. If the optical depth is divided small enough, the optical depth dependent absorption coefficient κ_n^* can be used to replace wavelength dependent absorption coefficient $\kappa(\lambda)$:

$$I_{n+1} = I_n e^{-\kappa_n^*(f_v)\Delta z} \tag{17}$$

This equation makes the photothermal conversion efficiency maintain the same:

$$\eta_n(\Delta z, f_v) = \frac{\int_{0.2\mu m}^{3um} E_n(\lambda)\left(1 - e^{-\kappa(\lambda, f_v)\Delta z}\right)d\lambda}{\int_{0.2\mu m}^{3um} E_n(\lambda)d\lambda} = \frac{I_{n+1} - I_n}{I_n} = 1 - e^{-\kappa_n^*(f_v)\Delta z} \quad (18)$$

So the optical depth dependent absorption coefficient can be calculated through:

$$\kappa_n^*(f_v) = -\frac{\ln\left(1 - \frac{\int_{0.2\mu m}^{3um} E_n(\lambda)\left(1 - e^{-\kappa(\lambda, f_v)\Delta z}\right)d\lambda}{\int_{0.2\mu m}^{3um} E_n(\lambda)d\lambda}\right)}{\Delta z} \quad (19)$$

The model is built in COMSOL Multiphysics®, using Radiation in Absorbing-Scattering Media model, where the optical depth dependent absorption coefficient is selected as a function of optical depth (z-direction). In order to validate the optical depth-dependent method proposed above, the radiative intensity distribution along the center line of gold nanofluid with concentration of 1 ppm under 10 sun is calculated through the original method and the proposed method, as shown in **Fig. 9**. The radiative intensity shows very good consistency for the two methods. What is noteworthy is that for the original method, the absorption coefficient and radiative intensity are both wavelength dependent (as shown in **Equation 13**), which dramatically increases the computing time and causes complicated modification of pre-defined radiative transfer equations inside commercial CFD software (COMSOL Multiphysics® in this paper). However, it can save more than 80% of the computing time when the optical depth-dependent method is employed.

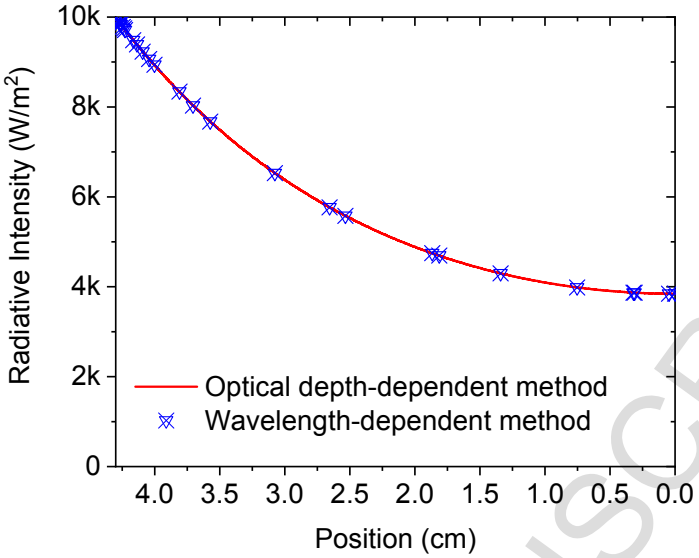

Fig. 9. Comparison of radiative intensity (center line, 1 ppm gold nanofluid under 10 sun) along the optical depth from optical depth-dependent method and wavelength-dependent method

Transient heat transfer equation is shown as:

$$\rho c_p \frac{\partial T}{\partial t} + \rho c_p \vec{u} \cdot \nabla T + \nabla \cdot \vec{q} + q_{\text{evap}} = Q_r \tag{20}$$

$$\vec{q} = -k \nabla T \tag{21}$$

$$Q_r = -q_\eta \tag{22}$$

where q_η is the radiative heat source, which is coupled by Multiphysics of HTRASM; q_{evap} is the boundary heat source which is only valid at the surface of nanofluid.

4.2. Evaporation and Moisture Transport

Nanofluid absorbs solar energy, which increases the temperature and accelerates the evaporation process. Evaporation of the surface of nanofluid releases latent heat of water and consumes the

converted thermal form from solar energy. The heat flux of evaporation depends on the amount of evaporated water, which can be described as:

$$q_{\text{evap}} = \text{L}g_{\text{evap}} \tag{23}$$

where L is the latent heat of vaporization and g_{evap} is the evaporative flux given in kg/s. The amount of water evaporated at the surface is obtained by Model of MT, where the evaporative flux at the surface is:

$$g_{\text{evap}} = \text{M}_\text{v}\frac{\partial((c_{\text{sat}} - c_v))}{\partial t} \tag{24}$$

where M_v is the molar mass of water vapor, c_v is the vapor concentration at the surface, c_{sat} is the saturation concentration which is related to the local pressure and temperature.

The moisture content variation can be described through the transport of vapor concentration as:

$$\text{M}_\text{v}\frac{\partial c_v}{\partial t} + \text{M}_\text{v}\vec{u}\cdot\nabla c_v + \nabla\cdot\left(-\text{M}_\text{v}D\nabla c_v\right) = G \tag{25}$$

where D is the vapor diffusion coefficient in air, $\vec{u}$ is the air velocity field and calculated from Multiphysics of MF, which couples the moisture transport and laminar flow. G is the moisture source which is g_{evap} at the surface of nanofluid.

The Laminar Flow model is employed to simulate the air and moisture flow inside the balance, where gravity force is considered in order to simulate the buoyancy force which is caused by density change with temperature. The Multiphysics of NITF and MF were added to couple with heat transfer and moisture transport in air.

4.3. Solution methodology

Equations 5-12 and 16-19 was numerically solved in MATLAB® and the optical depth dependent absorption coefficient $\kappa^*(z)$ was obtained for the next numerical model. The evaporation process under solar radiation of nanofluid was simulated through COMSOL

Multiphysics®. Before the simulation, various mesh numbers and time steps were tested for the independence verifications. The maximum element size was chosen as 0.2 cm, and the maximum element size was chosen as 0.02 cm at the evaporation surface. Non-structured mesh was used, which consisted of 402836 domain elements, 29204 boundary elements and 1856 edge elements. For the transient model, the time-step was chosen as 5 s in the solution, and the simulated temperature increase was smooth and well agreed with the experimental results. The discretization of the simulative space was conducted with the appliance of a built-in non-structured meshing COMSOL® algorithm. A direct solver called PARDISO® (parallel sparse direct solver) with a tolerance of 10^{-4} was adopted to numerically solve the matrices assembled according to the governing equations and boundary conditions described above. The initial and boundary conditions were originated from experimental measurement. The Advanced Research Computing (ARC) at University of Leeds is used to solve the equations in in parallel.

5. Numerical results and comparison

5.1. Validation against experimental data

As shown in **Fig. 10**, the temperature and evaporation rate from numerical results agrees well with experimental results. For water under 5 sun, the maximum difference of temperature and evaporation rate is within 5% and 3%, respectively. For 1 ppm gold nanofluid under 5 sun, the temperature of TC1~TC5 shows good agreement. However, in **Fig. 10B**, the temperature of TC6 from experiments is lower than that of simulative results after 30 minutes. The position of TC6 is slightly lower than the surface level of nanofluid at the beginning of experiments. During experiments, the level gradually descends due to water evaporation. In the numerical model, the liquid level is assumed to be fixed. After 30 minutes, the position of TC6 reaches approximately

the liquid level, where the temperature is lower than that under the level due to evaporative heat loss. This can be detailly explained in section 5.3.

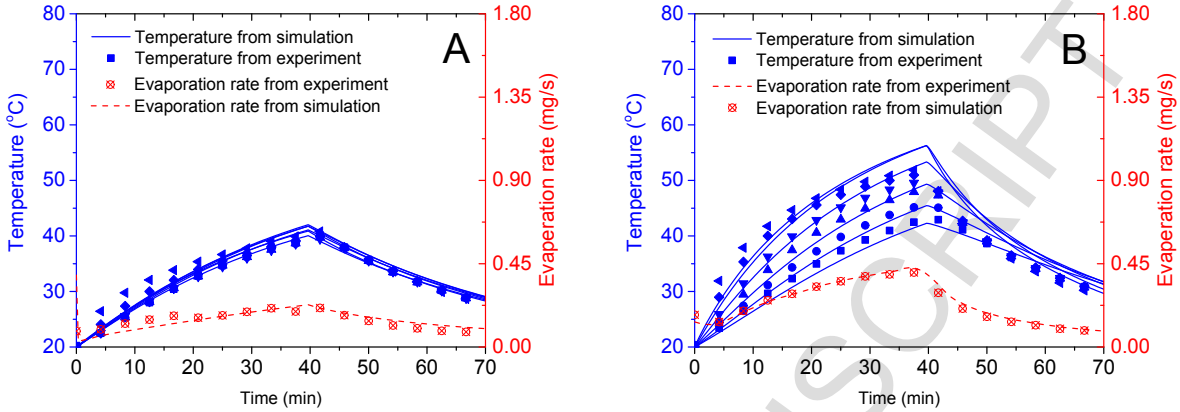

Fig. 10. Comparison between experimentally and numerically obtained temperature profile of TC1-TC6 and evaporation rate: (**A**) water under 5 sun (**B**) 1 ppm gold nanofluid under 5 sun

5.2. Temperature profile

The temperature profile can be seen from **Fig. 11** and **Fig. 12**. For water, the absorption coefficient was small due to relatively poor radiation trapping capability. The temperature of the vertical center line of water increased almost evenly with time, as shown in **Fig. 11A**. But for gold nanofluid, the temperature of near-surface increased much faster than that of the far bottom of fluid. As shown in **Fig. 11D**, the temperature of the surface reached about 65 ℃, but the temperature of the bottom was less than 30 ℃. The difference was more amplified when the concentration of nanofluid increased, which was consistent with the experimental results. This was more obvious from 2-D temperature profile from inset. What's more, the temperature of the bottom increased more slowly when the concentration increased (e.g., the bottom temperature was near 40 ℃ and 30 ℃ after 40 minutes for 1 ppm nanofluid and 12.5 ppm nanofluid, respectively). This is because that more solar energy is converted into thermal energy at the upper part of nanofluid, i.e., the thermal trapping of solar energy happenes at the top. When solar intensity is 10 sun, the

temperature difference between surface and bottom is more obvious. As shown in **Fig. 12**D, the temperature difference reaches 50 ℃ after 40 minutes. As shown **Fig. 12**C and **Fig. 12**D, the temperature of surface increases more slowly than that of the bottom after 30 minutes (i.e., 2.5 ℃ for the surface and 5 ℃ for the bottom in 10 minutes). When the temperature of surface reaches more than 80 ℃, convective and evaporative heat loss of the surface are comparable with radiative heat transfer, which causes the slow temperature increase.

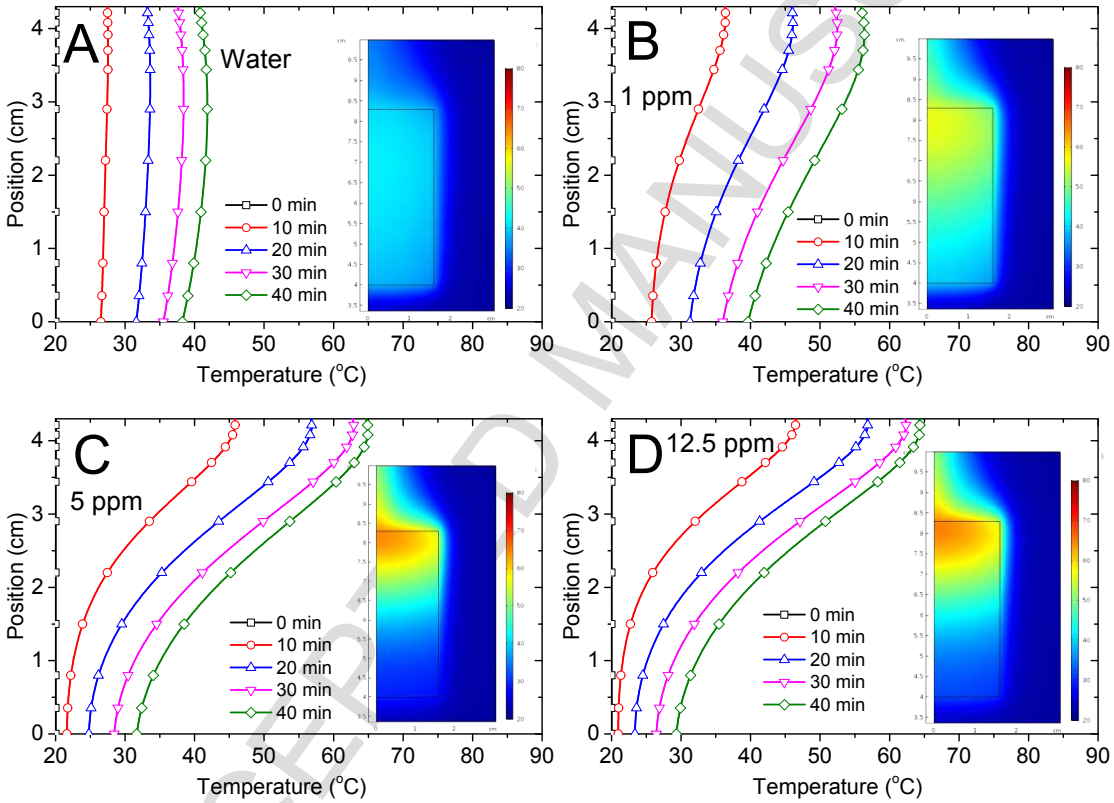

Fig. 11. Temperature change with time of the vertical center line of gold nanofluid under solar intensity of 5 sun: (**A**) water; (**B**) 1 ppm; (**C**) 5 ppm; (**D**) 12.5 ppm. The inset shows the temperature profile at 40 minutes from simulation

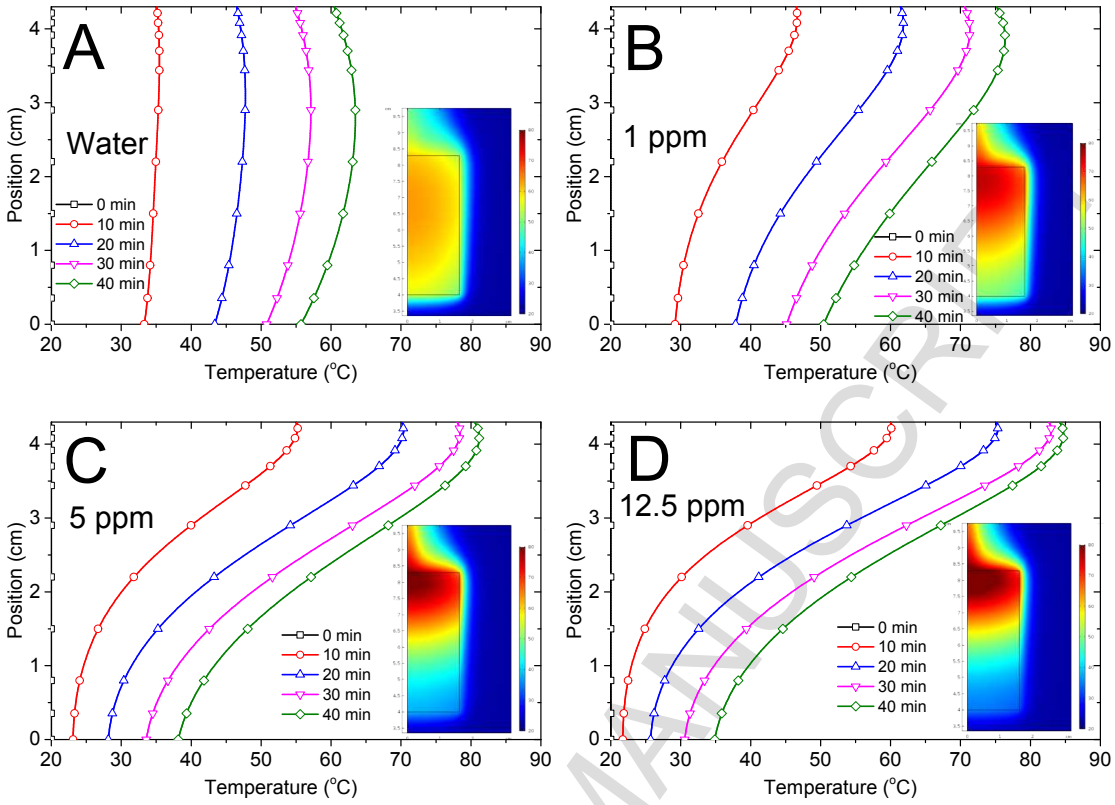

Fig. 12. Temperature change with time of the vertical center line of gold nanofluid under the solar intensity of 10 sun: (**A**) water; (**B**) 1 ppm; (**C**) 5 ppm; (**D**) 12.5 ppm. The inset shows the temperature profile at 40 minutes from simulation

5.3. Radiative intensity profile

The radiative intensity distribution is calculated through **Equation 13**. As shown in **Fig. 13** and **Fig. 14**, most of the solar energy goes through water, and nearly no absorption happens (i.e., the radiative intensity is nearly 5000 W/m^2 and 10000 W/m^2 along the optical depth for the incident intensity of 5 sun and 10 sun, respectively). When solar energy goes through gold nanofluid, radiative intensity decays significantly, i.e., most of the solar energy is converted into thermal form when passing through. Most of the solar energy is trapped in the surface area when the concentration of gold nanofluid is high enough. For instance, when the concentration is 12.5 ppm,

the incident intensity is 10000 W/m^2 as shown in **Fig. 14**, the intensity is reduced to less than 2500 W/m^2 at the center of nanofluid along the optical depth, which means more than 75% percent of solar energy is trapped in the top area. This's the reason why the surface temperature increases much faster than the bottom temperature as shown in **Fig. 11D** and **Fig. 12D**. From our previous research[44,52], the photothermal conversion efficiency is independent with solar intensity if the heat loss is negligible. For the same concentration (e.g., 12.5 ppm) as shown in **Fig. 13** and **Fig. 14**, the radiative intensity decreases with the same proportion along optical. When the concentration of nanofluid is higher than 5 ppm, the radiative intensity distribution is similar at the top part along optical depth (e.g., 12.5 ppm and 25 ppm). For gold nanofluid with a high concentration (e.g., > 5 ppm), most of the solar energy (e.g., $> 80\%$) was trapped even when the optical depth was 2 cm, leading to high photothermal conversion efficiency[52]. With the top part of nanofluid absorbs such a large amount of solar energy, the temperature of the surface increases much faster than that of the bottom. Additionally, the thermal conductivity of nanofluid in this paper (i.e., with a concentration of less than 25 ppm) is almost as low as that of water. This results in the large temperature gradient along the optical depth.

The saturation concentration of water increases with surface temperature, which finally increases the evaporation rate. According to the analysis above, the most efficient way to evaporate water is to concentrate more solar energy at the top part of nanofluid, i.e., increasing the concentration of nanofluid and trapping more radiative energy inside the top part. For the current experimental arrangement, the evaporation process happens only at the surface of the test samples. So for nanofluid especially with high concentrations, more solar energy is converted into latent heat instead of sensible heat, as shown in **Fig. 7**.

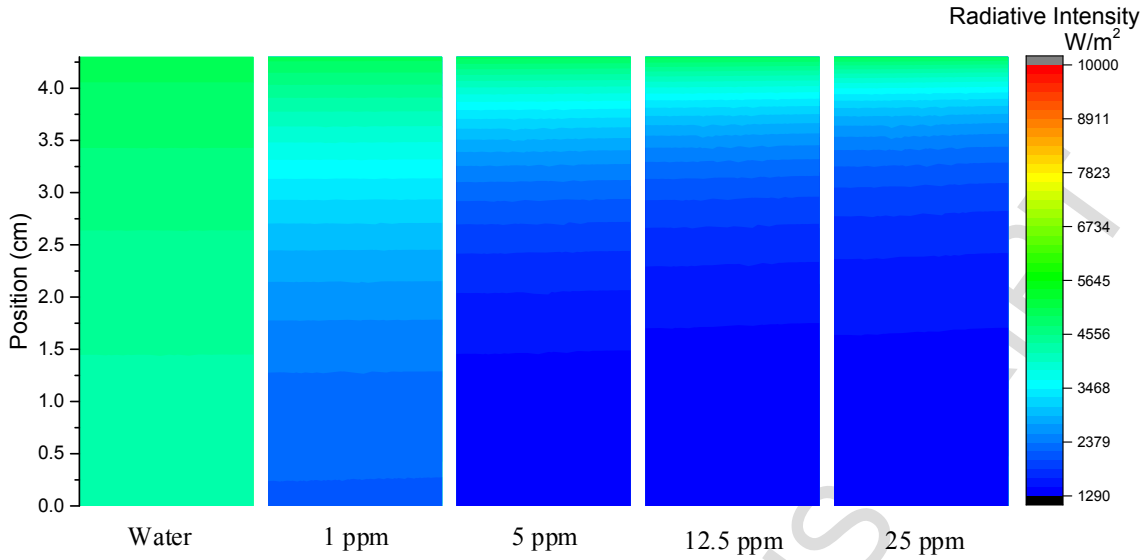

Fig. 13. The profile of radiative intensity at 40 minutes from the simulation for water and different concentration of gold nanofluid (the incident intensity is 5 sun)

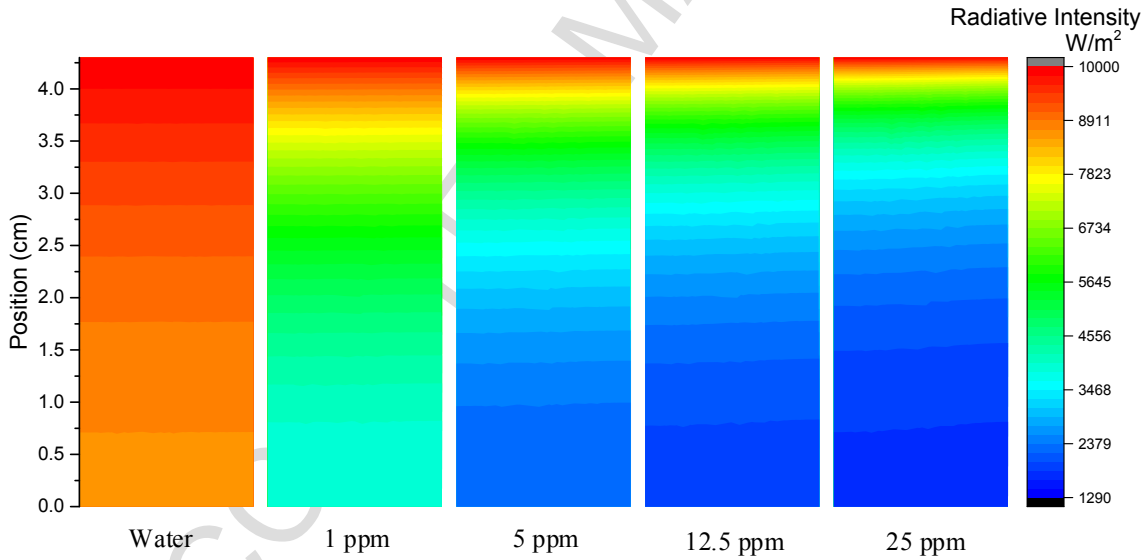

Fig. 14. The profile of radiative intensity at 40 minutes from the simulation for water and different concentration of gold nanofluid (the incident intensity is 10 sun)

5.4. Optimization for solar vapor generation

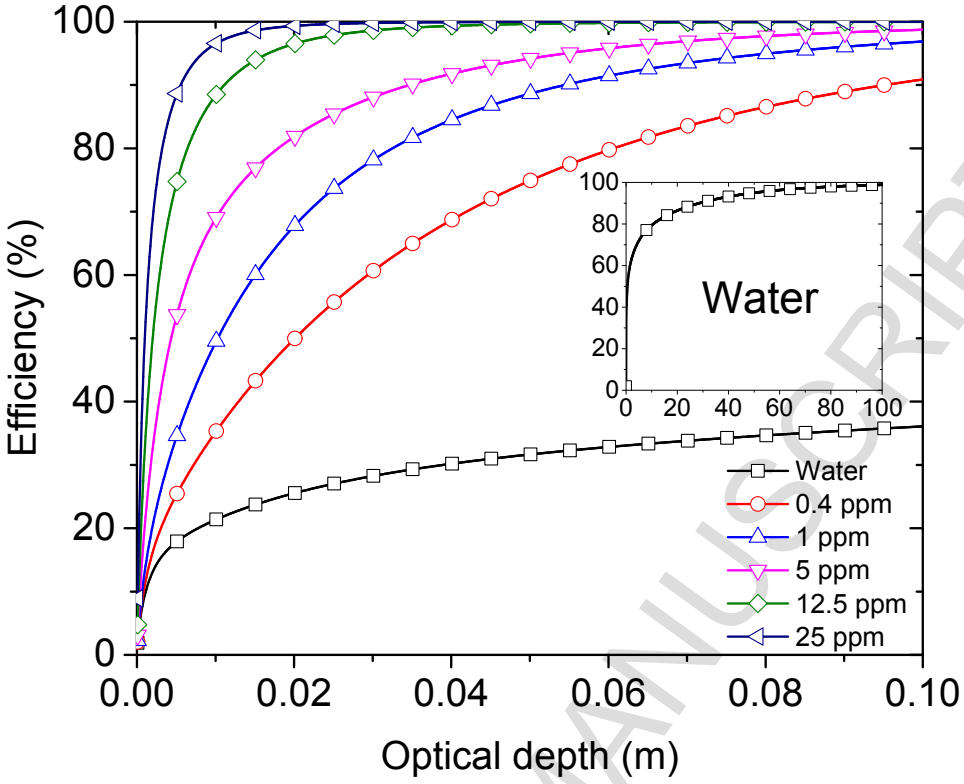

Fig. 15. Solar absorption efficiency as a function of optical depth for different volume concentrations of gold nanofluid

According to **Equation 16**, solar absorption efficiency is a function of optical depth and nanofluid concentration, which can be seen in **Fig. 15**. At the beginning, the efficiency increases rapidly with L, then asymptotically reaches 100%. As shown in radiative transfer equations (**Equation 13**), the radiative transport energy is consumed inside the nanofluid exponentially, and the absorption efficiency should exhibit a nonlinear dependence on the particle concentration. Actually, the absorption efficiency also reveals the important parameters that determine the maximum possible solar receiver efficiency. The impact of the optical depth L and particle concentration f_v is embedded in the exponential term as $L \cdot f_v$ in **Equation 16**. **Fig. 15** reveals that both particle concentration and optical depth should be in relatively small values to achieve

an optimized effect, as higher volume concentration of nanoparticle (i.e., more than 12.5 ppm for L=0.02 m) increases the efficiency slightly. For water, the efficiency depends more on the optical depth to reach a relative high value (i.e., 25 m for 80%).

As discussed above, in order to accelerate evaporation rate of solar vapor generation in the present arrangement, the most effective way is to trap more solar energy inside the top part of nanofluid. As shown in **Fig. 3CD** and **Fig. 4CD**, gold nanofluid with a concentration of 5 ppm and 12.5 ppm shows similar evaporation rate and temperature distribution. In fact, solar energy has been mostly trapped in the surface area (as shown in **Fig. 13** and **Fig. 14**), increasing concentration will not accelerate evaporation rate significantly. In order to optimize solar vapor generation, we define an optimal range of nanofluid concentration and optical depth, when the upper half of nanofluid absorbs 80%~90% of solar energy. For gold nanofluid, the optimal range can be seen in **Fig. 16**. For a certain optical depth, e.g., 4.3 cm in this experimental setting, the optimal concentration range of gold nanofluid is from 3.26 ppm to 6.89 ppm. If the concentration is less than 3.26 ppm, e.g., 1 ppm, some solar radiation passes through nanofluid (as shown in **Fig. 14**) and the trapped energy at the surface is less intense (as shown in **Fig. 4B**). This results the waste of solar energy in vapor generation. If the concentration is more than 6.89 ppm, e.g., 12.5 ppm in the current experiment, the solar energy is over trapped at the surface. As a result, the evaporation rate is almost the same with that of nanofluid with the concentration of 5 ppm, as shown in **Fig. 4CD**. For solar vapor generation, it is a waste of nanoparticles when over concentrated. For solar vapor generation, the optimal range varies with the different type of nanoparticles (e.g., material, shape and size). The optimization proposed can be a universally applicable method for solar vapor generation design. In the future application, a thin flowing layer of high concentration of nanofluid

(e.g., $L = 0.025$ m and $f_v = 12.5$ ppm gold nanofluid) will have high solar energy conversion efficiency and evaporation rate.

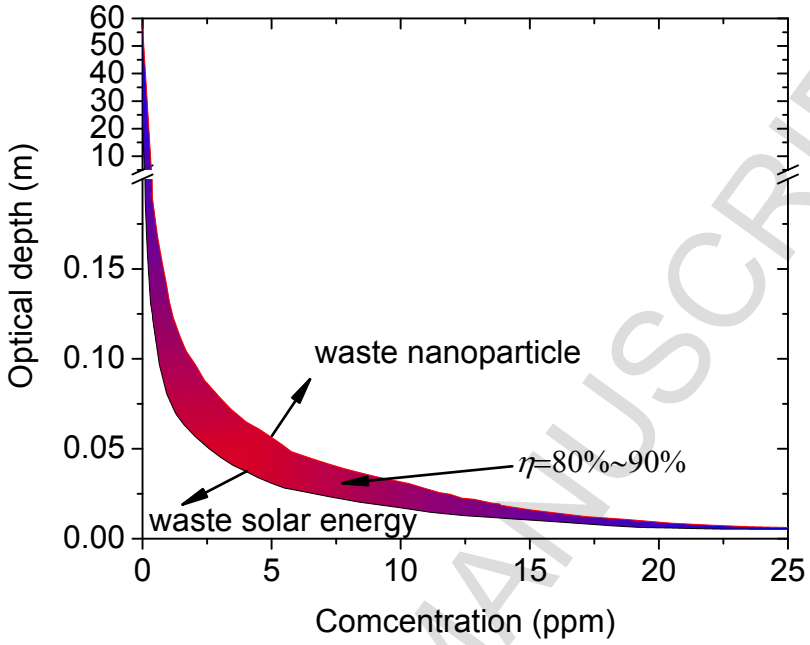

Fig. 16. Optimal range of nanofluid concentration and optical depth for solar vapor generation

6. Conclusions

Both experiments and simulation study were conducted in this work to analyze the nanoparticle-based solar vapor generation process. A new method was proposed to optimize the range of nanofluid concentration and optical depth. The main conclusions can be summarized as:

(1) The highest evaporation rate reached 0.65 mg/s for 12.5 ppm gold nanofluid, almost 3 times of that of DI water.

(2) Adding nanoparticles into fluid significantly increases total energy absorption from solar radiative energy. Gold nanoparticles inside water could increase photothermal conversion efficiency and evaporate more water with lower bulk temperature under the current experimental settings in this paper.

(3) Significant non-uniform temperature distribution was observed inside the fluid. Energy trapping at the surface of nanofluid was responsible for the fast vapor generation.

(4) A new method based on radiative transfer equation was proposed to predict energy efficiency. The optimal range of concentration of nanofluid and optical range was presented. The optimization proposed in this work can apply to other types of nanofluid for effective solar vapor generation.

Acknowledgments

This work was supported by the National Natural Science Foundation of China (No. 51776012), and the author Haichuan Jin also acknowledges the financial support for his visiting study at the University of Leeds from the China Scholarship Council (CSC) under the Grant No.201506020031. Aimen Zeiny gratefully acknowledges the Iraqi Ministry of Higher Education and Scientific Research for financial support (Grant No. 2001 in 12-05-2013).

References

[1] Neumann O, Urban AS, Day J, Lal S, Nordlander P, Halas NJ. Solar vapor generation enabled by nanoparticles. ACS Nano 2013;7:42–9. doi:10.1021/nn304948h.

[2] Gan Y, Qiao L. Optical properties and radiation-enhanced evaporation of nanofluid fuels containing carbon-based nanostructures. Energy and Fuels 2012;26:4224–30. doi:10.1021/ef300493m.

[3] Hogan NJ, Urban AS, Ayala-Orozco C, Pimpinelli A, Nordlander P, Halas NJ. Nanoparticles heat through light localization. Nano Lett 2014;14:4640–5. doi:10.1021/nl5016975.

[4] Ni G, Miljkovic N, Ghasemi H, Huang X, Boriskina S V., Lin C Te, et al. Volumetric solar heating of nanofluids for direct vapor generation. Nano Energy 2015;17:290–301. doi:10.1016/j.nanoen.2015.08.021.

[5] Li Tong W, Ong W-J, Chai S-P, Tan MK, Mun Hung Y. Enhanced Evaporation Strength through Fast Water Permeation in Graphene-Oxide Deposition. Sci Rep 2015;5:11896. doi:10.1038/srep11896.

[6] Neumann O, Feronti C, Neumann AD, Dong A, Schell K, Lu B, et al. Compact solar autoclave based on steam generation using broadband light-harvesting nanoparticles. Proc Natl Acad Sci 2013;110:11677–81. doi:10.1073/pnas.1310131110.

[7] Ishii S, Sugavaneshwar RP, Nagao T. Titanium Nitride Nanoparticles as Plasmonic Solar Heat Transducers. J Phys Chem C 2016;120:2343–8. doi:10.1021/acs.jpcc.5b09604.

[8] Zhou L, Tan Y, Ji D, Zhu B, Zhang P, Xu J, et al. Self-assembly of highly efficient, broadband plasmonic absorbers for solar steam generation. Sci Adv 2016;2:e1501227–e1501227. doi:10.1126/sciadv.1501227.

[9] Wang X, Ou G, Wang N, Wu H. Graphene-based Recyclable Photo-Absorbers for High-Efficiency Seawater Desalination. ACS Appl Mater Interfaces 2016;8:9194–9. doi:10.1021/acsami.6b02071.

[10] Zhao D, Duan H, Yu S, Zhang Y, He J, Quan X, et al. Enhancing Localized Evaporation through Separated Light Absorbing Centers and Scattering Centers. Sci Rep 2015;5:17276. doi:10.1038/srep17276.

[11] Ghasemi H, Ni G, Marconnet AM, Loomis J, Yerci S, Miljkovic N, et al. Solar steam generation by heat localization. Nat Commun 2014;5:4449. doi:10.1038/ncomms5449.

[12] Shannon MA, Bohn PW, Elimelech M, Georgiadis JG, Mariñas BJ, Mayes AM. Science and technology for water purification in the coming decades. Nature 2008;452:301–10. doi:10.1038/nature06599.

[13] Elimelech M, Phillip WA. The Future of Seawater Desalination: Energy, Technology, and the Environment. Science (80-) 2011;333:712–7. doi:10.1126/science.1200488.

[14] Gupta MK, Kaushik SC. Exergy analysis and investigation for various feed water heaters of direct steam generation solar-thermal power plant. Renew Energy 2010;35:1228–35. doi:10.1016/j.renene.2009.09.007.

[15] Tiwari GN, Singh HN, Tripathi R. Present status of solar distillation. Sol Energy 2003;75:367–73. doi:10.1016/j.solener.2003.07.005.

[16] Arai N, Itaya Y, Hasatani M. Development of a “volume heat-trap” type solar collector using a fine-particle semitransparent liquid suspension (FPSS) as a heat vehicle and heat storage medium Unsteady, one-dimensional heat transfer in a horizontal FPSS layer heated by thermal radiatio. Sol Energy 1984;32:49–56. doi:10.1016/0038-092X(84)90048-3.

[17] Mahian O, Kianifar A, Kalogirou SA, Pop I, Wongwises S. A review of the applications of nanofluids in solar energy. Int J Heat Mass Transf 2013;57:582–94. doi:10.1016/j.ijheatmasstransfer.2012.10.037.

[18] Taylor RA, Phelan P, Adrian R, Gunawan A, Otanicar T. Characterization of a Nanofluid Volumetric Solar Absorber/Steam Generator. ASME 2011 5th Int Conf Energy Sustain 2011:1927–36. doi:10.1115/ES2011-54062.

[19] Govorov AO, Richardson HH. Generating heat with metal nanoparticles. Nano Today 2007;2:30–8. doi:10.1016/S1748-0132(07)70017-8.

[20] Sanchot A, Baffou G, Marty R, Arbouet A, Quidant R, Girard C, et al. Plasmonic nanoparticle networks for light and heat concentration. ACS Nano 2012;6:3434–40. doi:10.1021/nn300470j.

[21] Shamshirgaran SR, Khalaji Assadi M, Badescu V, Al-Kayiem HH. Upper limits for the work extraction by nanofluid-filled selective flat-plate solar collectors. Energy 2018;160:875–85. doi:10.1016/J.ENERGY.2018.06.154.

[22] Lee S-H, Choi TJ, Jang SP. Thermal efficiency comparison: Surface-based solar receivers with conventional fluids and volumetric solar receivers with nanofluids. Energy 2016;115:404–17. doi:10.1016/J.ENERGY.2016.09.024.

[23] Loni R, Askari Asli-ardeh E, Ghobadian B, Kasaeian AB, Gorjian S. Thermodynamic analysis of a solar dish receiver using different nanofluids. Energy 2017;133:749–60. doi:10.1016/J.ENERGY.2017.05.016.

[24] Sharafeldin MA, Gróf G, Mahian O. Experimental study on the performance of a flat-plate collector using WO3/Water nanofluids. Energy 2017;141:2436–44. doi:10.1016/J.ENERGY.2017.11.068.

[25] Gan Y, Qiao L. Radiation-enhanced evaporation of ethanol fuel containing suspended metal nanoparticles. Int J Heat Mass Transf 2012;55:5777–82. doi:10.1016/j.ijheatmasstransfer.2012.05.074.

[26] Hussain I, Graham S, Wang Z, Tan B, Sherrington DC, Rannard SP, et al. Size-controlled synthesis of near-monodisperse gold nanoparticles in the 1-4 nm range using polymeric stabilizers. J Am Chem Soc 2005;127:16398–9. doi:10.1021/ja055321v.

[27] Hwang SH, Yun J, Jang J. Multi-shell porous TiO2 hollow nanoparticles for enhanced light harvesting in dye-sensitized solar cells. Adv Funct Mater 2014;24:7619–26. doi:10.1002/adfm.201401915.

[28] Mock JJ, Barbic M, Smith DR, Schultz DA, Schultz S. Shape effects in plasmon resonance of individual colloidal silver nanoparticles. J Chem Phys 2002;116:6755–9. doi:10.1063/1.1462610.

[29] Otanicar TP, Phelan PE, Prasher RS, Rosengarten G, Taylor RA. Nanofluid-based direct absorption solar collector. J Renew Sustain Energy 2010;2:033102. doi:10.1063/1.3429737.

[30] Lenert A, Wang EN. Optimization of nanofluid volumetric receivers for solar thermal energy conversion. Sol Energy 2012;86:253–65. doi:10.1016/j.solener.2011.09.029.

[31] Luo Z, Wang C, Wei W, Xiao G, Ni M. Performance improvement of a nanofluid solar collector based on direct absorption collection (DAC) concepts. Int J Heat Mass Transf 2014;75:262–71. doi:10.1016/j.ijheatmasstransfer.2014.03.072.

[32] Zhang H, Chen HJ, Du X, Wen D. Photothermal conversion characteristics of gold nanoparticle dispersions. Sol Energy 2014;100:141–7. doi:10.1016/j.solener.2013.12.004.

[33] Bandarra FEP, Mendoza OSH, Beicker CLL, Menezes A, Wen D. Experimental investigation of a silver nanoparticle-based direct absorption solar thermal system. Energy Convers Manag 2014;84:261–7. doi:10.1016/j.enconman.2014.04.009.

[34] Saidur R, Meng TC, Said Z, Hasanuzzaman M, Kamyar A. Evaluation of the effect of nanofluid-based absorbers on direct solar collector. Int J Heat Mass Transf 2012;55:5899–907. doi:10.1016/j.ijheatmasstransfer.2012.05.087.

[35] Fang Z, Zhen YR, Neumann O, Polman A, García De Abajo FJ, Nordlander P, et al. Evolution of light-induced vapor generation at a liquid-immersed metallic nanoparticle. Nano Lett 2013;13:1736–42. doi:10.1021/nl4003238.

[36] Govorov AO, Zhang W, Skeini T, Richardson H, Lee J, Kotov NA. Gold nanoparticle ensembles as heaters and actuators: Melting and collective plasmon resonances. Nanoscale Res Lett 2006;1:84–90. doi:10.1007/s11671-006-9015-7.

[37] Chen X, Munjiza A, Zhang K, Wen D. Molecular Dynamics Simulation of Heat Transfer from a Gold Nanoparticle to a Water Pool. J Phys Chem C 2014;118:1285–93. doi:org/10.1021/jp410054j.

[38] Baffou G, Quidant R, García De Abajo FJ. Nanoscale control of optical heating in complex plasmonic systems. ACS Nano 2010;4:709–16. doi:10.1021/nn901144d.

[39] Donner JS, Baffou G, McCloskey D, Quidant R. Plasmon-assisted optofluidics. ACS Nano 2011;5:5457–62. doi:10.1021/nn200590u.

[40] Lukianova E, Hu Y, Latterini L, Tarpani L, Lee S, Drezek RA, et al. Plasmonic nanobubbles as transient vapor nanobubbles generated around plasmonic nanoparticles. ACS Nano 2010;4:2109–23. doi:10.1021/nn1000222.

[41] Ma H, Bendix PM, Oddershede LB. Large-scale orientation dependent heating from a single irradiated gold nanorod. Nano Lett 2012;12:3954–60. doi:10.1021/nl3010918.

[42] Ye E, Win KY, Tan HR, Lin M, Teng CP, Mlayah A, et al. Plasmonic gold nanocrosses with multidirectional excitation and strong photothermal effect. J Am Chem Soc 2011;133:8506–9. doi:10.1021/ja202832r.

[43] Baffou G, Bon P, Savatier J, Polleux J, Zhu M, Merlin M, et al. Thermal imaging of nanostructures by quantitative optical phase analysis. ACS Nano 2012;6:2452–8. doi:10.1021/nn2047586.

[44] Jin H, Lin G, Bai L, Zeiny A, Wen D. Steam generation in a nanoparticle-based solar receiver. Nano Energy 2016;28:397–406. doi:10.1016/j.nanoen.2016.08.011.

[45] Huang J, He Y, Hu Y, Wang X. Steam generation enabled by a high efficiency solar absorber with thermal concentration. Energy 2018;165:1282–91. doi:10.1016/J.ENERGY.2018.10.099.

[46] Amjad M, Jin H, Du X, Wen D. Experimental photothermal performance of nanofluids under concentrated solar flux. Sol Energy Mater Sol Cells 2018;182:255–62. doi:10.1016/j.solmat.2018.03.044.

[47] Zeiny A, Jin H, Bai L, Lin G, Wen D. A comparative study of direct absorption nanofluids for solar thermal applications. Sol Energy 2018;161:74–82. doi:10.1016/j.solener.2017.12.037.

[48] Zeiny A, Jin H, Lin G, Song P, Wen D. Solar evaporation via nanofluids: A comparative study. Renew Energy 2018;122:443–54. doi:10.1016/j.renene.2018.01.043.

[49] Chen H, Wen D. Ultrasonic-aided fabrication of gold nanofluids. Nanoscale Res Lett 2011;6:198. doi:10.1186/1556-276X-6-198.

[50] Modest MF. Radiative Heat Transfer. vol. 1. Academic Press; 2003. doi:http://dx.doi.org/10.1016/B978-012503163-9/50021-7.

[51] Moffat RJ. Describing the uncertainties in experimental results. Exp Therm Fluid Sci 1988;1:3–17. doi:10.1016/0894-1777(88)90043-X.

[52] Jin H, Lin G, Bai L, Amjad M, Bandarra Filho EP, Wen D. Photothermal conversion efficiency of nanofluids: An experimental and numerical study. Sol Energy 2016;139:278–89. doi:10.1016/j.solener.2016.09.021.

[53] Gueymard CA. The sun's total and spectral irradiance for solar energy applications and solar radiation models. Sol Energy 2004;76:423–53. doi:10.1016/j.solener.2003.08.039.

[54] McPeak KM, Jayanti S V., Kress SJP, Meyer S, Iotti S, Rossinelli A, et al. Plasmonic films can easily be better: Rules and recipes. ACS Photonics 2015;2:326–33. doi:10.1021/ph5004237.

[55] Babar S, Weaver JH. Optical constants of Cu, Ag, and Au revisited. Appl Opt 2015;54:477. doi:10.1364/AO.54.000477.

[56] Hale GM, Querry MR. Optical Constants of Water in the 200-nm to 200-μm Wavelength Region. Appl Opt 1973;12:555. doi:10.1364/AO.12.000555.

Research Highlights:

- Solar vapor generation has been investigated both experimentally and numerically.
- Localized energy trapping is responsible for the fast vapor generation.
- The recommended range of nanofluid concentration and optical depth are proposed.